Dalton Transactions

ROYAL SOCIETY OF CHEMISTRY

PAPER

View Article Online
View Journal

Cite this: DOI: 10.1039/d5dt00726g

Bipolaron hopping conduction in vacancy-ordered Cs_2PtI_6 perovskites

Vidya Raj, [a,b] Abhishek Anand, [a,b] Manasa Manoj[a,b] and Aravind Kumar Chandiran *[a,b]

Received 25th March 2025,
Accepted 10th August 2025

DOI: 10.1039/d5dt00726g

rsc.li/dalton

Among vacancy-ordered perovskites, Cs_2PtI_6 exhibits remarkable efficiency and stability, making it a promising material for photovoltaic and photoelectrochemical applications. However, further advancements require a comprehensive understanding of its charge conduction and relaxation mechanisms, which remain insufficiently explored. This study investigates these mechanisms through temperature-dependent impedance and Raman spectroscopic techniques. Activation energy analysis from conductivity data and temperature-dependent Raman spectroscopy suggests polaronic type conduction. The frequency exponent trend from AC conductivity reveals that correlated barrier hopping is the primary charge conduction mechanism, with the isolated octahedra in the structure acting as barriers for polaron hopping. Enhanced conductivity at higher temperatures is attributed to energy gained by carriers to overcome potential barriers for conduction and increased hopping rates. X-ray photoemission spectroscopy reveals the presence of mixed Pt oxidation states (Pt^{2+} and Pt^{4+}), and the phonon-assisted charge transfer between them supports bipolaron redox-mediated conduction.

Introduction

Vacancy-ordered halide perovskites have emerged as a stable and non-toxic alternative to conventional organic–inorganic halide perovskites. This class of halide perovskites $A_2B'\square X_6$ (A – monovalent cation, B′ – tetravalent cation, □ – cation vacancy and X – halide) are created by replacing two divalent cations (B) in ABX_3 with a tetravalent atom (B′), resulting in a vacant cationic site.[1] Although discovered years ago, research into their applicability across different applications remains in its early stages.[2–4] In 2014, the vacancy-ordered perovskite Cs_2SnI_6, with a direct bandgap of 1.3–1.6 eV, was first introduced for photovoltaic applications in dye-sensitized solar cells, achieving a power conversion efficiency (PCE) of approximately 4–6%.[4–7] Subsequently, it was employed as an absorber layer in perovskite solar cells, where it demonstrated an efficiency of around 1%.[8–13] Doping with SnF_2 has further enhanced the PCE to 5.18%.[14] However, the limited efficiency of Cs_2SnI_6 is primarily attributed to its low electron mobility (~3 $cm^2\ V^{-1}\ s^{-1}$), high resistivity (in the MΩ range), and significant defect density (>10^{19} cm^{-3}).[11,15] Although Cs_2SnX_6 has been explored for photovoltaic and photoelectrochemical applications, its poor long-term stability renders it unsuitable for practical use.[16] Another class of vacancy-ordered perovskites, Cs_2TiX_6, with a bandgap of ~1.8 eV, has demonstrated a PCE of 3.3% in photovoltaic applications.[2] While the photovoltaic potential of other vacancy-ordered perovskites, such as tellurium-based compounds, has been theoretically predicted, no experimental devices have been reported to date.[17–21]

Among vacancy-ordered materials, Cs_2PtI_6 stands out by achieving the highest reported efficiency of 13.88%, attributed to its narrow bandgap (1.37 eV) and high absorption coefficient (~4 × 10^5 cm^{-1}).[3] Its exceptional stability under acidic and basic conditions, high temperatures, and electrochemical environments has made it a promising candidate both as a photoanode for water oxidation and as a high-performance photovoltaic material.[3,16,22–24] Theoretical models suggest that with optimized device architecture, Cs_2PtI_6 could reach efficiencies exceeding 20%.[25,26] Moreover, it has been shown to be biocompatible with microorganisms, expanding its potential in photoelectrochemical applications.[27] Despite its excellent ambient and pH stability, there is still significant room for performance enhancement in photovoltaic and photoelectrochemical applications.[22–24,28–31] To achieve this, understanding its charge conduction mechanism is crucial and these studies in this class of materials have not been explored. This study aims to address that gap by investigating the charge conduction and relaxation mechanisms in Cs_2PtI_6 through temperature-dependent impedance and Raman spectroscopic measurements. The experimental procedure for the synthesis of the materials and its basic characterization data are provided in SI.

[a]Department of Chemical Engineering, Indian Institute of Technology Madras, Adyar, Chennai, Tamil Nadu 600036, India. E-mail: aravindkumar@iitm.ac.in
[b]Hyundai HTWO Innovation Centre, Indian Institute of Technology Madras, Adyar, Chennai, Tamil Nadu 600036, India

Impedance spectroscopy is a powerful technique for understanding the electrical and dielectric behavior of a material. In this method, a sinusoidal perturbation is applied, and the corresponding AC response is recorded. From this response, impedance and related parameters as a function of frequency are calculated.

Impedance is a complex quantity represented as

$$Z* = Z' + jZ'' \quad (1)$$

where Z' is the real part and Z'' is the imaginary part of the impedance. Temperature-dependent impedance measurements have been conducted on Cs_2PtI_6 pellets to understand their dynamic response under varying electric fields.

Results and discussion

The Nyquist plots (Z' *versus* Z'') of Cs_2PtI_6 at different temperatures are illustrated in Fig. S1(a–c). The impedance spectra at all temperatures were fitted using the equivalent circuit model R_1 + (R_2‖CPE$_2$) + (R_3‖CPE$_3$) in Z-view software. In this model, R_1 represents the series resistance, attributed to parasitic losses such as contact and wiring resistance. The R_2‖CPE$_2$ element represents the impedance associated with the bulk, while R_3‖CPE$_3$ corresponds to the grain boundary impedance.[32,33] The resistive components reflect energy dissipation in the form of heat. A Constant Phase Element (CPE) is used in place of an ideal capacitor to account for the non-ideal capacitive behavior caused by sample inhomogeneity and distributed relaxation times. As the temperature increases from 100 K to 400 K, both R_2 and R_3 decrease substantially—from 200 GΩ to 70 kΩ and 500 GΩ to 250 kΩ, respectively—indicating reduced resistivity in both the bulk and grain boundary regions (Fig. S1(d)). Notably, grain boundary resistance remains higher than bulk resistance.[34]

The real and imaginary parts of impedance provide complementary insights into a material's electrical behavior, with the real part reflecting resistive effects and the imaginary part capturing capacitive or inductive contributions. Separately analyzing these components is essential for a comprehensive understanding. The real part of impedance (Z') is closely linked to the material's DC resistance and offers valuable information about conduction pathways. To investigate the frequency-dependent resistive behavior, Z' has been plotted against frequency (Fig. 1(a)). A reduction in impedance with increasing temperature is evident (as observed in Fig. S1(d)), and for clarity, the temperature dependence of Z' at 1 Hz is shown in Fig. 1(b). In Fig. 1(a), the frequency dependence of Z' displays distinct trends at different temperature ranges. At higher temperatures, Z' exhibits two regions: a frequency-independent plateau at lower frequencies, corresponding to the DC resistance, followed by a decrease in resistance with increasing frequency (inset of Fig. 1(a)). In contrast, at lower temperatures (150 K ≤ T ≤ 100 K), the trend is entirely different: Z' decreases steeply across the entire frequency range. At higher temperatures, sufficient thermal energy is available to charge carriers, resulting in frequency-independent conduction up to a certain frequency. Beyond this frequency, the availability of more charge carriers for conduction causes a steep reduction in Z'. In contrast, at lower temperatures, the limited thermal energy restricts charge carrier mobility, making conduction predominantly frequency-dependent. These findings highlight the strong dependence of resistive effects on both temperature and frequency.

While Z' describes the conduction behavior, Z'' provides insights into the relaxation behavior in the material. The frequency dependent Z'' plot shows peaks that correspond to a specific relaxation behavior. The relaxation time is time taken by the charge carriers to come back to its equilibrium after it is perturbed by an alternating electric field. The relaxation time (τ) is obtained from the peak frequency (f_{max}) using the relation:

$$\tau = 1/\omega_{max} = 1/2\pi f_{max}. \quad (2)$$

In Cs_2PtI_6, the imaginary part of impedance (Z'') displays a single relaxation peak that shifts to higher frequencies with increasing temperature (Fig. 1(c)). As the temperature rises from 100 K to 400 K, the relaxation time decreases from seconds to microseconds, as shown in Fig. S2. This indicates that with more thermal energy, the increased mobility of charge carriers facilitate faster relaxation of the material. Thus, a temperature-dependent primary relaxation process exists in this material.

By analyzing the temperature dependence of the relaxation time, the activation energy of the underlying relaxation mechanism can be determined using the Arrhenius relation:[35]

$$\tau = \tau_0 \exp(-E_A/k_B T) \quad (3)$$

The activation energy provides insights into the dominant charge carrier or relaxation mechanism in a material, such as charge carrier hopping, dipole reorientation, or polarization relaxation.[36–38] In Cs_2PtI_6, data fitting reveals two activation energies at different temperature regimes, as shown in Fig. 1(d). The activation energy is 0.095 eV at higher temperatures and 0.062 eV at lower temperatures. The presence of two activation energies suggest that the relaxation mechanism changes with temperature. At lower temperatures, the relaxation is possibly due to slow-moving ions or localized polarons. However, as the temperature increases, faster-moving ions or polaron hopping mechanisms become involved.[39,40] Therefore, in Cs_2PtI_6, the relaxation mechanism is a complex phenomenon, influenced by multiple charge carriers in different temperature regimes.

At low frequencies, the material may exhibit capacitive behavior, allowing the capacitance to be extracted from Z^*, where Z^* is represented as:

$$Z* = 1/j\omega C* \quad (4)$$

where C^* is the capacitance of the material ($C = \varepsilon^* A/d$, A is the area of the plates, d is the distance between the plates, and ε^* is the dielectric permittivity). Using eqn (4), the temperature

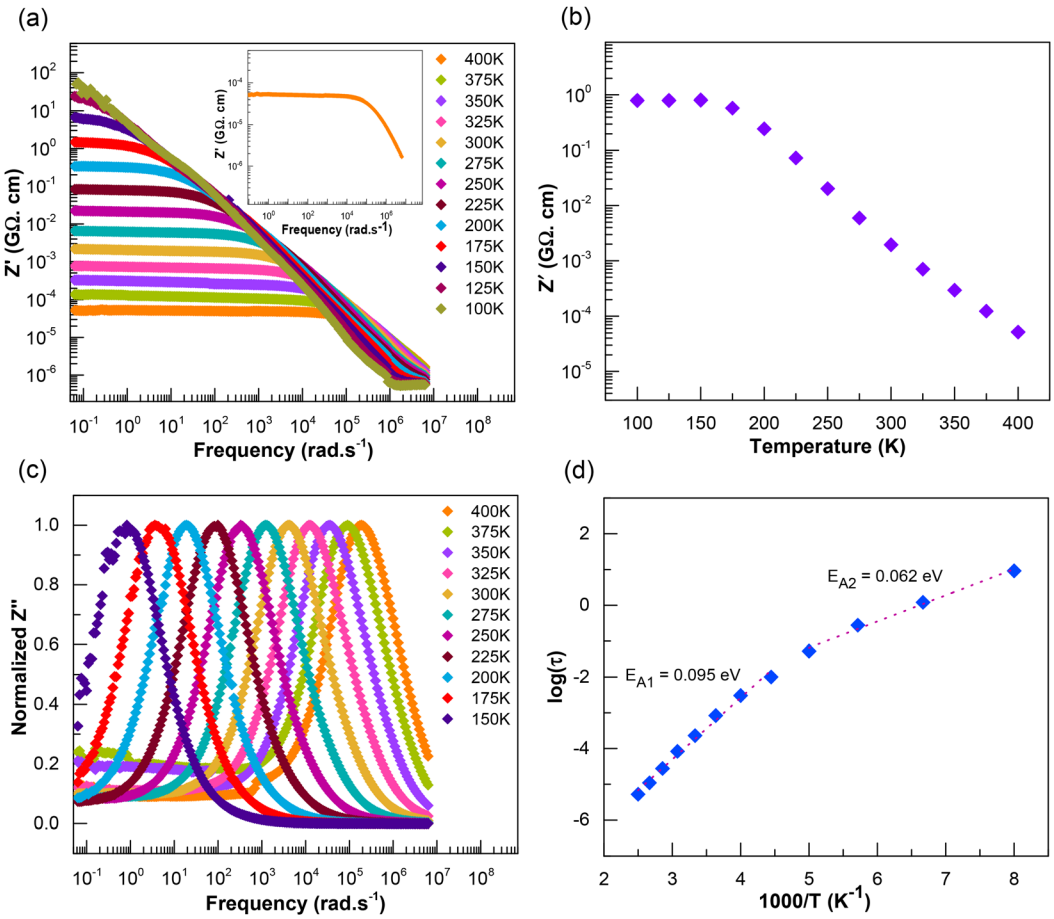

Fig. 1 (a) Variation of the real part of impedance (Z') plots of Cs_2PtI_6, measured over a temperature range of 400 K to 100 K and a frequency range of 1 MHz to 10 MHz, with temperature steps of 25 K. The inset depicts the variation in Z' as a function of frequency at 400 K. (b) Variation of the real part of impedance (Z') with temperature, plotted with a logarithmic y-axis, measured at 1 Hz. (c) Imaginary part of impedance (Z'') *versus* frequency at different temperatures. (d) Extraction of activation energies from the relaxation time in two temperature regimes using the Arrhenius relation.

and frequency-dependent dielectric permittivity can be extracted from Z^*, which aids in understanding the energy storage and dissipation properties of Cs_2PtI_6 under various conditions. This analysis also helps identify potential relaxation processes. The complex permittivity is expressed as:[41]

$$\varepsilon* = \varepsilon' - j\varepsilon'' \quad (5)$$

where ε' represents the real part of complex permittivity (dielectric constant) and ε'' denotes the imaginary part of complex permittivity (dielectric loss).

$$\varepsilon' = -Z''/[\omega C_0(Z'^2 + Z''^2)] \quad (6)$$

$$\varepsilon'' = Z'/[\omega C_0(Z'^2 + Z''^2)] \quad (7)$$

The real part of permittivity reflects the material's ability to store energy under an applied external electric field. Fig. 2(a) shows the frequency-dependent dielectric constant at different temperatures. The plot exhibits two distinct steps, one at lower frequencies and the other at higher frequencies. At low frequencies, charge carriers can effectively respond to the slowly varying electric field, resulting in higher charge storage and, consequently, a higher dielectric constant. In contrast, at high frequencies, the applied electric field changes too rapidly for the charge carriers to keep up, causing a decrease in the dielectric constant with increasing frequency.[42] As the temperature increases, sufficient energy becomes available to activate more charge carriers, leading to a higher dielectric constant. Fig. 2(b) illustrates the increase in dielectric constant with rising temperature at 10 MHz. However, at very high frequencies, all the plots converge, as the charge carriers can no longer respond to the rapid changes in the electric field. At this point, the dielectric constant becomes independent of temperature. The dielectric constant provides information about the polarizability of a material, while dielectric loss quantifies the energy dissipated as heat when the material is exposed to a varying electric field. Similar to the dielectric constant, dielectric loss also increases with temperature due to enhanced phonon activity (Fig. 2(c)).[43] At low frequencies, charge carriers can move freely, resulting in greater heat dissipation. In contrast, at high frequencies, the rapid variations in the electric field prevents charge carriers from responding, leading to lower heat losses.[44] The temperature-dependent be-

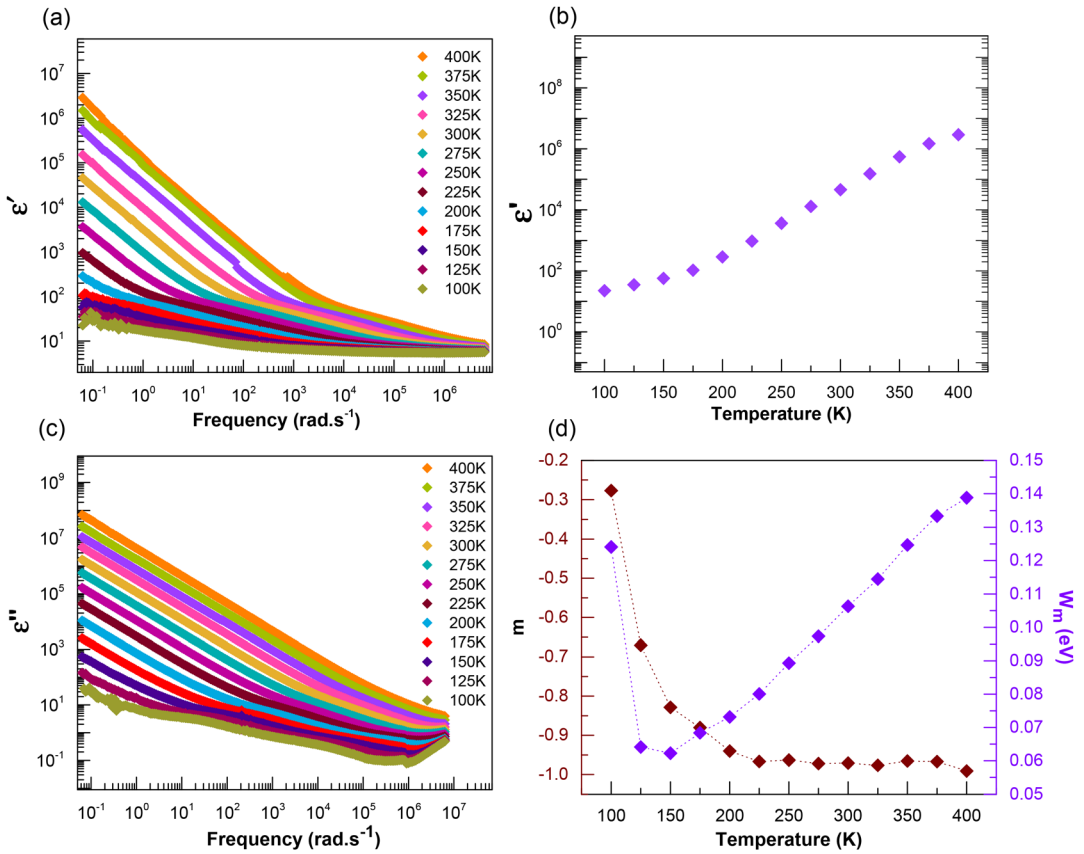

Fig. 2 (a) Temperature-dependent dielectric permittivity (ε') as a function of frequency. (b) Variation of the real part of dielectric permittivity (dielectric constant) with temperature at 10 MHz. (c) Temperature-dependent trend of the imaginary part of dielectric permittivity (dielectric loss) with temperature. (d) Variation of the parameter m and W_m with temperature.

havior of dielectric loss is explained by the Stevels model, which highlights the interaction between charge carriers and lattice phonons:

$$\varepsilon'' = A'\omega^m \tag{8}$$

Here A' is the constant of proportionality, ω is the angular frequency and m is the slope of the dielectric loss *versus* frequency curve (<0). The slope 'm' indicates the interaction between the dipoles,

$$m = -4k_BT/W_m \tag{9}$$

where W_m is the barrier height for charge conduction, representing the energy needed for charge carriers to overcome the barriers and participate in conduction. The barrier height for charge carriers in Cs_2PtI_6 as a function of temperature is determined from the slope 'm' of the low-frequency step and is depicted in Fig. 2(d). The temperature rise essentially decreases the value of 'm'. The W_m on the other hand initially decreases between 100 K and 150 K but further increase in temperature continues to raise the barrier height. Although the barrier height increases, the resistance to charge conduction decreases by several orders of magnitude (as shown in Fig. S1). This is possibly due to enhanced mobility of carriers at high temperatures as they obtain sufficient energy to overcome the barrier.

Due to its soft nature, Cs_2PtI_6 is anticipated to demonstrate diverse types of conduction such as ionic, electronic, and dipolar. Analyzing the frequency-dependent behavior of conductivity is crucial for distinguishing between these conduction mechanisms. The total conductivity of Cs_2PtI_6 has been calculated from the impedance data as follows:[45]

$$\sigma = (t/A'')(Z'/(Z'^2 + Z''^2)) \tag{10}$$

where t is thickness and A'' is the area of the pellets.

Fig. 3(a) shows the conductivity plots of Cs_2PtI_6 over a temperature range of 400–100 K. In the lower temperature regime ($T \leq 150$ K), conductivity is frequency-dependent and increases with rising frequency. On contrast to that, at higher temperatures, the conductivity displays two distinct regions: a low-frequency, frequency-independent plateau and a high-frequency dispersion region where conductivity increases with frequency. This behavior of conductivity follows Jonscher's power law:[46,47]

$$\sigma(\omega) = \sigma_{DC}(\omega) + \sigma_{AC}(\omega). \tag{11}$$

The first term, $\sigma_{DC}(\omega)$, represents the DC conductivity, which is frequency-independent. It represents the electronic or ionic-charge conduction ability of the material under the influ-

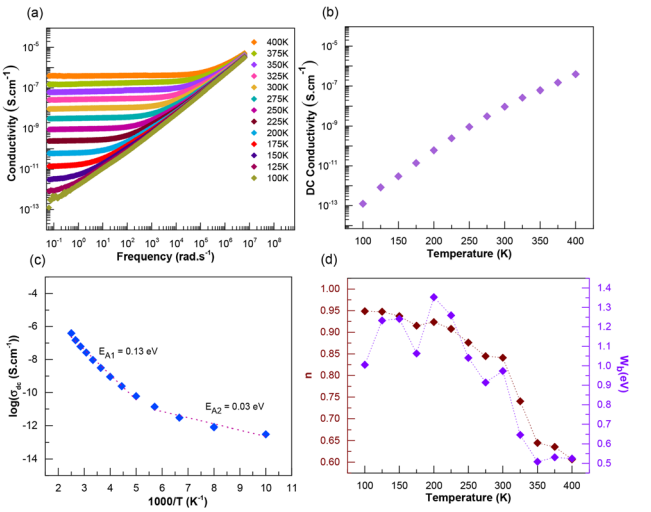

Fig. 3 (a) The temperature-dependent conductivity variation with respect to frequency. (b) The variation of DC conductivity with temperature. (c) The extraction of activation energies from DC conductivity at two temperature regimes using the Arrhenius relation. (d) The variation of frequency exponent and binding energy with temperature.

ence of an applied electric field. The second term, $\sigma_{AC}(\omega)$, is frequency-dependent and is attributed to dielectric relaxation resulting from localized or trapped charge carriers.[41] The frequency-dependence of AC conductivity is expressed as:

$$\sigma_{AC}(\omega) = A\omega^{n} \quad (12)$$

where A is the dispersion parameter, ω is the angular frequency and n is the frequency exponent ($0 \leq n \leq 1$). The parameter A is temperature-dependent and measures polarizability (Fig. S3(a)). An increase in 'A' with rising temperature indicates higher polarizability of the material at elevated temperatures. At low frequencies, conductivity is primarily due to the DC component, which depends on the available free charge carriers. The frequency at which the transition from DC conductivity to AC conductivity occurs is known as the hopping frequency (ω_H). The hopping frequency of charge carriers between localized states increases with rising temperature, as represented in Fig. S3(b). Thus, the increase in DC conductivity from 0.1 pS cm^{-1} to 0.1 μS cm^{-1} with temperature rise from 100 to 400 K (Fig. 3(b)) is mainly attributed to increased charge carrier mobility and hopping rate. This increase in conductivity with temperature suggests semiconductor behavior and a thermally-activated conduction mechanism. The activation energies for charge conduction in two different temperature regimes are determined from the Arrhenius relation between DC conductivity and temperature, as shown in Fig. 3(c).

$$\sigma_{DC}(\omega) = \sigma_0 \exp(-E_A/k_B T) \quad (13)$$

Here, σ_0 represents the pre-exponential factor, and E_A is the activation energy. The activation energies are determined to be 0.13 eV and 0.03 eV at higher and lower temperatures, respectively. The activation energy obtained from conductivity data specifies the energy required for the long-range transport of the charge carriers.[41,48] The activation energy derived from the relaxation mechanism represents the energy necessary for the localized relaxation of charge carriers, such as their reorientation or polarization within the material.[49] In contrast, the activation energy calculated from conductivity data corresponds to the energy barrier for the excitation of additional charge carriers in the lattice.[50] These two mechanisms reflect different aspects of charge transport behavior and are influenced differently by temperature and material structure.[41,49,50] In the case of conductivity, the disparity in activation energies between low and high temperatures is more pronounced. At lower temperatures, electrical conduction primarily involves electronic charge carriers, which require less energy to move. As the temperature rises, additional mechanisms—such as the movement of ionic species and the activation of previously trapped charge carriers—begin to contribute significantly to the conduction process. These mechanisms generally involve higher energy barriers, thus leading to a substantial increase in activation energy at elevated temperatures. On the other hand, relaxation phenomena are inherently more localized, involving processes like dipolar reorientation or short-range hopping, which do not require extensive charge carrier transport across the material.[51] As a result, the difference in activation energies for relaxation processes between low and high temperatures is relatively small. This comparatively minor variation reflects the localized nature of polarization or carrier relaxation. Therefore, we propose that the reason for the larger energy difference observed in conductivity measurements, compared to relaxation processes, is due to the fundamentally different nature of the two mechanisms—long-range transport *versus* localized relaxation—and their respective sensitivities to structural and thermal changes in the material. The obtained activation energy values are in good agreement with previously reported values for polaron hopping in halide perovskites.[50,52–54]

Temperature-dependent Raman spectroscopy measurements offer insights into structural and vibrational changes associated with polaron conduction. Raman spectra of Cs_2PtI_6 pellets were recorded at temperatures ranging from 125 K to 325 K, as illustrated in Fig. 4(a). The spectra exhibit two distinct peaks: one between 148 cm^{-1} and 152 cm^{-1}, attributed to the A_{1g} vibrational mode corresponding to Pt–I symmetric stretch, and another between 127 cm^{-1} and 130 cm^{-1}, assigned to the E_g vibrational mode corresponding to Pt–I asymmetric stretch.[5] Gaussian function fitting was applied to these peaks to determine the full width at half-maximum (FWHM) and peak positions. As temperature increases from 125 K to 325 K, both the width and position of these peaks undergo significant changes, while the overall spectral pattern remains largely consistent within this temperature range. All bands shift to lower wavenumbers and broaden with rising temperatures (Fig. 4(b and c)). The red shift observed in the bands with increasing temperature is attributed to lattice expansion, which leads to the formation of polarons.[55] The full width at half maximum (FWHM) of the A_{1g} mode increased from 1.7 cm^{-1} at 125 K to 3.5 cm^{-1} at 325 K, while

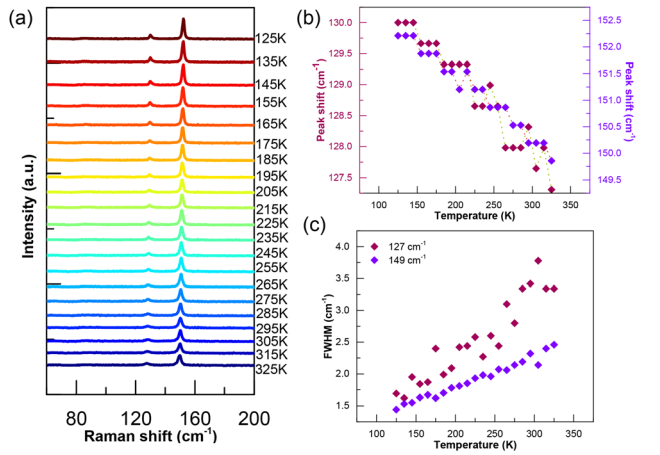

Fig. 4 (a) Temperature-dependent Raman spectroscopy in the temperature range of 325 K ≤ T ≤ 125 K. (b) The shift in the peak position with respect to temperature. (c) Change in the peak with change in temperature.

the FWHM of the E_g mode increased from 1.3 cm^{-1} at 125 K to 2.5 cm^{-1} at 325 K, indicating a decrease in phonon lifetime.[56,57] The increase in FWHM or decrease in phonon lifetime with temperature rise clearly indicates enhanced phonon–electron interaction, giving rise to polaron, with increasing temperature.

The frequency exponent (n) in eqn (12) is a temperature-dependent parameter that provides information about the interaction of moving charge carriers with the lattice. Its trend with temperature also reveals the underlying conduction mechanism. Several conduction mechanisms have been reported in the literature, including quantum mechanical tunneling (QMT), correlated barrier hopping (CBH), non-overlapping small polaron tunneling (NSPT), and overlapping large polaron tunneling (OLPT). In the QMT model, the frequency exponent n remains nearly constant around 0.8 or shows a slight increase with temperature. This mechanism involves tunneling of polarons between localized states without the need for thermal activation, and is typically dominant at low temperatures.[58] In the OLPT model, the value of n initially decreases with increasing temperature, reaches a minimum, and then begins to rise again. This behavior is attributed to the overlap of potential wells between hopping sites for large polarons, which reduces the energy required for hopping. As a result, large polarons are only weakly localized.[49,59,60] In the NSPT model, n increases with temperature. Here, small polarons are strongly localized due to significant coupling between charge carriers and lattice vibrations (phonons).[54,61–66] Conversely, in the CBH model, the value of n decreases as temperature increases. This mechanism involves thermally activated hopping over potential barriers that are correlated with the distance between localized sites.[67,68]

To determine the conduction mechanism in Cs_2PtI_6, the frequency exponent n was obtained from the slope of the AC conductivity curve at each temperature by fitting the linear region. The value of n is close to unity at 100 K, and as the temperature increases, the frequency exponent decreases. This trend suggests that Correlated Barrier Hopping (CBH) involving small polarons is the dominant conduction mechanism in Cs_2PtI_6 (Fig. 3(d)).[69,70]

Here, charge carriers must overcome potential barriers for conduction, likely associated with isolated octahedra in vacancy-ordered Cs_2PtI_6 perovskites. The isolated octahedra in Cs_2PtI_6 serve as centers for trapping polarons, leading to localized hopping of polarons to neighboring sites under an applied electric field, thereby causing dielectric relaxation. The deconvoluted fitted data of X-ray photoemission spectroscopy (Fig. S4) shows the coexistence of both Pt^{4+} and Pt^{2+} species in Pt 4f spectra, indicating the potential for redox-mediated polaron conduction in Cs_2PtI_6:

$$Pt^{2+} - 2e^- \rightarrow Pt^{4+}. \quad (14)$$

During electron hopping, a polarization cloud accompany the charge carrier, resulting in the formation of a polaron, as illustrated in Fig. 5(a). A bipolaron conduction mechanism is proposed in Cs_2PtI_6, where two electrons are transferred during conduction. As charge conduction primarily takes place through the CBH mechanism, polarons hop between adjacent octahedra in Cs_2PtI_6, where the barrier height is influenced by the distance between these octahedra. Consider a two-site scenario with two potential wells separated by a distance 'R' (Fig. 5(b)). Here, the vacancies in the ordered perovskite structure serves to define the barrier height for polarons hopping to neighboring potential wells. Polaron hopping occurs as the overlap between adjacent potential wells reduces the barrier height from W_m to W or when the carriers gain sufficient energy at high T to overcome the barrier:[71]

$$W = W_m - eq^2/\pi\varepsilon\varepsilon_0 R \quad (15)$$

where W_m is the maximum barrier height between adjacent potential wells (migration energy), e is the number of electrons

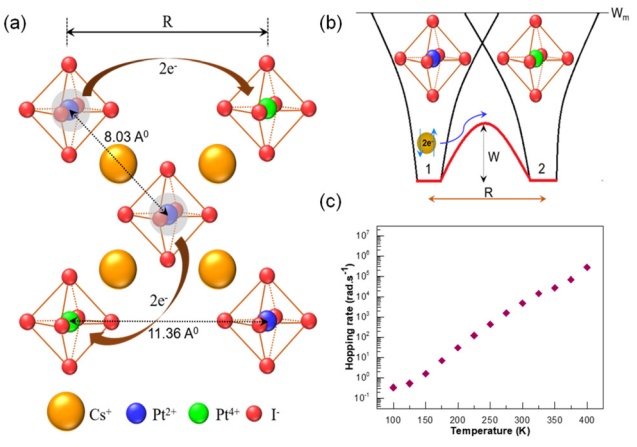

Fig. 5 (a) The polaron hopping mechanism in the isolated octahedron of Cs_2PtI_6 vacancy-ordered perovskites. (b) Correlated Barrier Hopping (CBH) mechanism between two octahedral sites of barrier height 'W'. (c) Increase in hopping rate of polarons with temperature.

participating in hopping (e = 1 for single polaron hopping and e = 2 for bipolaron hopping), R is the distance between potential wells, q is the electronic charge, ε_0 is the absolute permittivity of free space and ε is the dielectric permittivity.[72] The second term in the equation is the potential energy due to the coulombic interaction between localized charge carriers. The distinction between single and bipolaron hopping is based on the number of electrons involved in the hopping process between two defect states. If only one electron participates, the mechanism is referred to as single polaron hopping; if two electrons are involved simultaneously, it is known as bipolaron hopping.[70,73–78] Bipolaron hopping typically dominates at lower temperatures, and as the temperature increases, a transition to single polaron hopping can occur. This transition is often accompanied by a reduction in the barrier height (W_m), reflecting the lower energy required for single polaron movement at elevated temperatures.[73,79] Bipolaron hopping is closely associated with the Correlated Barrier Hopping (CBH) model, which has been found to be applicable to Cs_2PtI_6.[71,80] The closer the spacing of potential wells (R), the more efficient the hopping. Due to octahedral voids in Cs_2PtI_6, higher activation energy is required for hopping conduction. Elevated temperature and higher frequency both facilitate polaron hopping between adjacent lattice sites by providing sufficient energy to overcome barriers. The applied electric field too affects the distribution of polarons across localized sites. Hopping rate is defined as the frequency at which AC conductivity doubles that of DC conductivity.[81] As illustrated in Fig. 5(c), hopping rate increases exponentially with rising temperature. The increased hopping rate may result from a reduction in 'R' due to structural deformation at higher temperatures. The hopping mechanism can involve either long-range inter-well hopping or short-range intra-well hopping. Inter-well hopping occurs between adjacent potential wells, affecting DC conductivity, while intra-well hopping occurs within a potential well, influencing AC conductivity.[82,83] In CBH conduction mechanism, the frequency exponent is expressed as:[79,84]

$$n = 1 - (6k_BT/W_b) \quad (16)$$

where W_b is the binding energy needed for the movement of charge carrier from one site to another. The binding energy is calculated using eqn (16). With increasing temperature, the binding energy decreases (Fig. 3(d)) and consequently, at higher temperatures, more charge carriers can overcome the potential barriers and hop between sites.

Conclusions

In conclusion, temperature-dependent impedance and Raman spectroscopic measurements were done to investigate the charge conduction behavior in vacancy-ordered Cs_2PtI_6 perovskites. The activation energy extracted from DC conductivity suggests polaronic conduction as a plausible mechanism. Conductivity analysis follows Jonscher's law, from which the frequency exponent is derived, confirming the presence of the correlated barrier hopping mechanism in Cs_2PtI_6. Thus, temperature-activated polaron hopping between adjacent defect states, facilitated by isolated octahedra, is identified as the primary charge conduction mechanism in Cs_2PtI_6. This hopping mechanism depends on both temperature and the frequency of the applied field. At higher temperatures, faster carrier relaxation is observed, resulting in a higher hopping rate. X-ray photoemission spectroscopy confirms the presence of multiple oxidation states of Pt, demonstrating the transfer of two electrons between Pt^{2+} and Pt^{4+}, thereby supporting the proposal of a bipolaron redox-mediated conduction mechanism in Cs_2PtI_6.

Conflicts of interest

There are no conflicts to declare.

Data availability

All the required data are provided in the SI: structural characterization data, thermal, optical and impedance properties of materials. See DOI: https://doi.org/10.1039/d5dt00726g.

Acknowledgements

VR acknowledges the partial financial support from Indian Institute of Technology Madras through Institute Postdoctoral Fellowship. The project is partially funded by Indian Institute of Technology Madras through Institute of Eminence grant.

References

1 M. T. Anderson, K. B. Greenwood, G. A. Taylor and K. R. Poeppelmeier, *Prog. Solid State Chem.*, 1993, **22**, 197–233.
2 M. Chen, M.-G. Ju, A. D. Carl, Y. Zong, R. L. Grimm, J. Gu, X. C. Zeng, Y. Zhou and N. P. Padture, *Joule*, 2018, **2**, 558–570.
3 D. Schwartz, R. Murshed, H. Larson, B. Usprung, S. Soltanmohamad, R. Pandey, E. S. Barnard, A. Rockett, T. Hartmann and I. E. Castelli, *Phys. Status Solidi RRL*, 2020, **14**, 2000182.
4 B. Lee, C. C. Stoumpos, N. Zhou, F. Hao, C. Malliakas, C.-Y. Yeh, T. J. Marks, M. G. Kanatzidis and R. P. Chang, *J. Am. Chem. Soc.*, 2014, **136**, 15379–15385.
5 A. Kaltzoglou, M. Antoniadou, A. G. Kontos, C. C. Stoumpos, D. Perganti, E. Siranidi, V. Raptis, K. Trohidou, V. Psycharis and M. G. Kanatzidis, *J. Phys. Chem. C*, 2016, **120**, 11777–11785.
6 L. Peedikakkandy, J. Naduvath, S. Mallick and P. Bhargava, *Mater. Res. Bull.*, 2018, **108**, 113–119.

7 H. Shin, B. M. Kim, T. Jang, K. M. Kim, D. H. Roh, J. S. Nam, J. S. Kim, U. Y. Kim, B. Lee and Y. Pang, *Adv. Energy Mater.*, 2019, **9**, 1803243.
8 X. Qiu, B. Cao, S. Yuan, X. Chen, Z. Qiu, Y. Jiang, Q. Ye, H. Wang, H. Zeng, J. Liu and M. G. Kanatzidis, *Sol. Energy Mater. Sol. Cells*, 2017, **159**, 227–234.
9 X. Qiu, Y. Jiang, H. Zhang, Z. Qiu, S. Yuan, P. Wang and B. Cao, *Phys. Status Solidi RRL*, 2016, **10**, 587–591.
10 J. Zhang, S. Li, P. Yang, W. Liu and Y. Liao, *J. Mater. Sci.*, 2018, **53**, 4378–4386.
11 S. T. Umedov, D. B. Khadka, M. Yanagida, A. Grigorieva and Y. Shirai, *Sol. Energy Mater. Sol. Cells*, 2021, **230**, 111180.
12 X. Qiu, B. Cao, S. Yuan, X. Chen, Z. Qiu, Y. Jiang, Q. Ye, H. Wang, H. Zeng and J. Liu, *Sol. Energy Mater. Sol. Cells*, 2017, **159**, 227–234.
13 X. Qiu, Y. Jiang, H. Zhang, Z. Qiu, S. Yuan, P. Wang and B. Cao, *Phys. Status Solidi RRL*, 2016, **10**, 587–591.
14 R. Murshed, S. Thornton, C. Walkons, J. J. Koh and S. Bansal, *Sol. RRL*, 2023, **7**, 2300165.
15 W. Meng, X. Wang, Z. Xiao, J. Wang, D. B. Mitzi and Y. Yan, *J. Phys. Chem. Lett.*, 2017, **8**, 2999–3007.
16 M. Hamdan and A. K. Chandiran, *Angew. Chem., Int. Ed.*, 2020, **59**, 16033–16038.
17 M. Scholz, M. Morgenroth, A. Merker, K. Oum and T. Lenzer, *J. Phys. Chem. C*, 2023, **127**, 17871–17879.
18 R. Sa, Y. Wei, W. Zha and D. Liu, *Chem. Phys. Lett.*, 2020, **754**, 137538.
19 Y. Zhou, Y. Sun, L. Tu, Y. Gao, M. Lai, Y. Wan and J. Xu, *Phys. Scr.*, 2025, **100**, 045958.
20 B. Pal, A. J. Kale, M. Sharma, K. Bhamu, S. G. Kang, V. K. Singh and A. Dixit, *Energy Fuels*, 2024, **38**, 1430–1451.
21 I. Vazquez-Fernandez, S. Mariotti, O. S. Hutter, M. Birkett, T. D. Veal, T. D. Hobson, L. J. Phillips, L. Danos, P. K. Nayak and H. J. Snaith, *Chem. Mater.*, 2020, **32**, 6676–6684.
22 J. P. Jayaraman, M. Hamdan, M. Velpula, N. S. Kaisare and A. K. Chandiran, *ACS Appl. Mater. Interfaces*, 2021, **13**, 16267–16278.
23 M. Hamdan, M. Manoj, J. S. Halpati and A. K. Chandiran, *Sol. RRL*, 2022, **6**, 2101092.
24 S. Yang, L. Wang, S. Zhao, A. Liu, Y. Zhou, Q. Han, F. Yu, L. Gao, C. Zhang and T. Ma, *ACS Appl. Mater. Interfaces*, 2020, **12**, 44700–44709.
25 A. Amjad, S. Qamar, C. Zhao, K. Fatima, M. Sultan and Z. Akhter, *RSC Adv.*, 2023, **13**, 23211–23222.
26 A. H. H. Khan, M. Waqas and A. A. Khan, *Mater. Lett.: X*, 2025, **25**, 100241.
27 S. Shinde, M. Hamdan, P. Bhalla and A. K. Chandiran, *ACS Eng. Au*, 2023, **4**, 224–230.
28 M. Hamdan and A. K. Chandiran, *Angew. Chem.*, 2020, **132**, 16167–16172.
29 S. S. Padelkar, Vikram, J. J. Jasieniak, A. N. Simonov and A. Alam, *Phys. Rev. Appl.*, 2024, **21**, 044031.
30 N. Shanmugam, J. S. Halpati and A. K. Chandiran, *Adv. Mater. Interfaces*, 2023, **10**, 2201526.
31 M. Hamdan, M. Manoj, J. S. Halpati and A. K. Chandiran, *Sol. RRL*, 2022, **6**, 2101092.
32 S. Ullah, A. Andrio, J. Marí-Guaita, H. Ullah, A. Méndez-Blas, R. M. del Castillo Vázquez, B. Mari and V. Compañ, *Phys. Chem. Chem. Phys.*, 2024, **26**, 6736–6751.
33 A. Zohar, N. Kedem, I. Levine, D. Zohar, A. Vilan, D. Ehre, G. Hodes and D. Cahen, *J. Phys. Chem. Lett.*, 2016, **7**, 191–197.
34 S. Karmakar, *arXiv*, 2024, preprint, arXiv:2406.15467, DOI: **10.48550/arXiv.2406.15467**.
35 D. K. Pradhan, R. Choudhary and B. Samantaray, *Mater. Chem. Phys.*, 2009, **115**, 557–561.
36 S. Brahma, R. Choudhary and A. K. Thakur, *Phys. B*, 2005, **355**, 188–201.
37 B. Singh and B. Kumar, *Cryst. Res. Technol.*, 2010, **45**, 1003–1011.
38 W. Chen, W. Zhu, O. Tan and X. Chen, *J. Appl. Phys.*, 2010, **108**, 034101.
39 C. Wang and L. Zhang, *New J. Phys.*, 2007, **9**, 210.
40 I. Coondoo, N. Panwar, R. Vidyasagar and A. L. Kholkin, *Phys. Chem. Chem. Phys.*, 2016, **18**, 31184–31201.
41 K. S. Hemalatha, G. Sriprakash, M. V. N. Ambika Prasad, R. Damle and K. Rukmani, *J. Appl. Phys.*, 2015, **118**, 154103.
42 B. Quan, X. Liang, G. Ji, Y. Cheng, W. Liu, J. Ma, Y. Zhang, D. Li and G. Xu, *J. Alloys Compd.*, 2017, **728**, 1065–1075.
43 M. A. Dar, K. Majid, K. M. Batoo and R. Kotnala, *J. Alloys Compd.*, 2015, **632**, 307–320.
44 J. Tahalyani, K. K. Rahangdale, R. Aepuru, B. Kandasubramanian and S. Datar, *RSC Adv.*, 2016, **6**, 36588–36598.
45 S. Karoui and S. Kamoun, *Int. J. Sci. Res.*, 2015, **4**, 2201–2210.
46 A. K. Jonscher, *Nature*, 1977, **267**, 673–679.
47 A. K. Jonscher, *J. Phys. D: Appl. Phys.*, 1999, **32**, R57.
48 M. Idrees, M. Nadeem and M. Hassan, *J. Phys. D: Appl. Phys.*, 2010, **43**, 155401.
49 A. Sahoo, T. Paul, P. Pal, N. H. Makani, A. Ghosh and R. Banerjee, *Phys. Rev. Appl.*, 2023, **20**, 034024.
50 N. H. Makani, A. Sahoo, P. Pal, T. Paul, L. S. Tanwar, M. Singh, A. Ghosh and R. Banerjee, *Phys. Rev. Mater.*, 2022, **6**, 115002.
51 D. Emin, *Phys. Rev. B*, 1971, **4**, 3639.
52 R. Paul, N. K. Tailor, A. Mahaptra, P. Yadav and S. Satapathi, *J. Phys. D: Appl. Phys.*, 2022, **55**, 415301.
53 N. K. Tailor, N. Parikh, P. Yadav and S. Satapathi, *J. Phys. Chem. C*, 2022, **126**, 10199–10208.
54 N. K. Tailor, S. K. Saini, P. Yadav, M. Kumar and S. Satapathi, *J. Phys. Chem. Lett.*, 2023, **14**, 730–736.
55 P. Jain, M. Mazumder, K. Pradeep, R. Viswanatha, S. K. Pati and C. Narayana, *ACS Appl. Mater. Interfaces*, 2022, **14**, 5567–5577.
56 M. Kuball, J. Hayes, Y. Shi and J. Edgar, *Appl. Phys. Lett.*, 2000, **77**, 1958–1960.
57 N. Domènech-Amador, R. Cuscó, L. Artus, T. Yamaguchi and Y. Nanishi, *Phys. Rev. B: Condens. Matter Mater. Phys.*, 2011, **83**, 245203.

58 A. Ghosh, *Phys. Rev. B: Condens. Matter Mater. Phys.*, 1990, **41**, 1479.
59 N. Chakchouk, K. B. Brahim, M. B. Gzaiel and A. Oueslati, *RSC Adv.*, 2022, **12**, 6831–6840.
60 A. Long, *Adv. Phys.*, 1982, **31**, 553–637.
61 S. Nasri, A. B. Hafsia, M. Tabellout and M. Megdiche, *RSC Adv.*, 2016, **6**, 76659–76665.
62 K. Shan, D. Dastan, Z.-Z. Yi, M. K. Mohammed, X.-T. Yin, A. Timoumi and A. S. Weidenbach, *RSC Adv.*, 2023, **13**, 8683–8691.
63 Y. Fu, P.-Y. Wang, F. Wang, H. Wuliji, H. Zhu and J. Wang, *ACS Appl. Mater. Interfaces*, 2024, **16**, 15073–15083.
64 D. Pokhrel, S. Sahu, H. K. Singh, M. Tangi, V. Sridhar and D. Pamu, *Phys. Scr.*, 2024, **100**, 015911.
65 M. B. Bechir and F. Alresheedi, *RSC Adv.*, 2023, **13**, 34703–34714.
66 M. Krimi, F. Hajlaoui, M. S. Abdelbaky, S. Garcia-Granda and A. B. Rhaiem, *RSC Adv.*, 2024, **14**, 10219–10228.
67 A. Bougoffa, E. Benali, A. Benali, M. Bejar, E. Dhahri, M. Graça, M. Valente, G. Otero-Irurueta and B. Costa, *RSC Adv.*, 2022, **12**, 6907–6917.
68 N. Kanabar, K. Gadani, V. Shrimali, K. Sagapariya, K. Rathod, B. Udeshi, J. Joseph, D. Pandya, P. Solanki and N. Shah, *Appl. Phys. A*, 2021, **127**, 1–11.
69 M. Dult, R. Kundu, J. Hooda, S. Murugavel, R. Punia and N. Kishore, *J. Non-Cryst. Solids*, 2015, **423**, 1–8.
70 S. Elliott, *Philos. Mag.*, 1977, **36**, 1291–1304.
71 G. Pike, *Phys. Rev. B*, 1972, **6**, 1572.
72 A. Saleh, S. Hraibat, R.-L. Kitaneh, M. Abu-Samreh and S. Musameh, *J. Semicond.*, 2012, **33**, 082002.
73 S. Chatterjee and T. K. Kundu, *Phys. Scr.*, 2024, **100**, 015960.
74 A. Tawansi, A. El-Khodary, A. Oraby and A. Youssef, *J. Appl. Polym. Sci.*, 2005, **95**, 1333–1341.
75 V. Krinichnyi, H.-K. Roth, G. Hinrichsen, F. Lux and K. Lüders, *Phys. Rev. B: Condens. Matter Mater. Phys.*, 2002, **65**, 155205.
76 P. Brahma, S. Banerjee, S. Chakraborty and D. Chakravorty, *J. Appl. Phys.*, 2000, **88**, 6526–6528.
77 I. Elhamdi, F. Mselmi, H. Souissi, S. Kammoun, E. Dhahri, P. Sanguino and B. Costa, *RSC Adv.*, 2023, **13**, 3377–3393.
78 Y. Onodera, *Phys. Rev. B: Condens. Matter Mater. Phys.*, 1984, **30**, 775.
79 J. Koshy, S. M. Soosen, A. Chandran and K. George, *J. Semicond.*, 2015, **36**, 122003.
80 M. El-Nahass, H. Zeyada, M. El-Samanoudy and E. El-Menyawy, *J. Phys.: Condens. Matter*, 2006, **18**, 5163.
81 M. Shah, M. Nadeem and M. Atif, *J. Appl. Phys.*, 2012, **112**, 103718.
82 U. Akgul, Z. Ergin, M. Sekerci and Y. Atici, *Vacuum*, 2007, **82**, 340–345.
83 V. Biju and M. A. Khadar, *J. Mater. Sci.*, 2003, **38**, 4055–4063.
84 R. Jana, J. Datta, S. Sil, A. Dey, B. Pal, A. Biswas and P. P. Ray, *Mater. Res. Express*, 2019, **6**, 1050d1.